Impact of blockers on user equipment angular diversity in THz Microcellular scenarios

Jorge Gomez-Ponce*†, Naveed A. Abbasi*, Shadi Abu-Surra[‡], Gary Xu[‡], Charlie Zhang[‡], Andreas F. Molisch*

*University of Southern California, Los Angeles, CA, USA

†ESPOL Polytechnic University, Guayaquil, Ecuador

[‡]Samsung Research America, Richardson, TX, USA

Email: {gomezpon, nabbasi, molisch}@usc.edu,

{shadi.as, gary.xu, jianzhong.z}@samsung.com

Abstract—The availability of large bandwidths in the terahertz (THz) band will be a crucial enabler of high data rate applications in next-generation wireless communication systems. The urban microcellular scenario is an essential deployment scenario where the base station (BS) is significantly higher than the user equipment (UE). Under practical operating conditions, moving objects (i.e., blockers) can intermittently obstruct various parts of the BS-UE link. Therefore, in the current paper, we analyze the effect of such blockers. We assume a blockage of the strongest beam pair and investigate the availability and extent of angular diversity, i.e., alternative beampairs that can sustain communication when the strongest is blocked. The analysis uses double-directional channel measurements in urban microcellular scenarios for 145-146 GHz with BS-UE distances between 18 to 83 m. We relate the communication-system quantities of beam diversity and capacity to the wireless propagation conditions. We show that the SNR loss due to blockage depends on the blocked angular range and the specific location, and we find mean blockage loss to be on the order of 10-20 dB in line-of-sight (LOS) and 5-12 dB in NLOS (non-LOS). This analysis can contribute to the design of intelligent algorithms or devices (e.g., beamforming, intelligent reflective surfaces) to overcome the impact of the blockage.

Index Terms—Terahertz (THz) communication, microcell, urban scenario, angular diversity

I. INTRODUCTION

Data rate requirements for communication systems are ever increasing, and the support for new and upcoming applications such as virtual reality and immersive 3D environments is already becoming challenging under the current 5G wireless systems [1]. In this context, the terahertz (THz) band, with vast swaths of unused spectrum, is an important candidate for future wireless communication systems, and it has seen significant interest recently [2], [3].

The design of any wireless system requires detailed channel measurements representative of the scenario of interest. This is especially true for higher frequencies, such as the THz band, where the channel characteristics are currently poorly understood. A critical scenario of interest for THz channels is the microcellular scenario where the transmitter (Tx) is at an elevated height (usually greater than 10 m) in comparison to the receiver (Rx). From a measurement point of view, most existing channel measurements in the THz domain focus on indoor scenarios (see [3] and references therein); however, recently, there has been some progress on longer distances

and outdoor scenarios as well. These include the first long-distance (100 m) double-directional channel measurements for the 140 GHz band, which were reported in 2019 [4] by our group, as well as our recent works [5], [6] where we target device-to-device (D2D) and microcell scenarios for the first time in literature. Recent work by NYU [7] also reports THz measurements and statistical analysis at 140 GHz over Tx-Rx distances in an urban scenario where Tx is placed at 4 m above the ground (i.e., typical lamppost height).

However, the existing directionally resolved measurements were - due to the measurement principle of mechanically rotating horn antennas - done (as far as possible) in static environments, absent of moving scatterers/blockers such as pedestrians, cars, and buses that typically are encountered in urban environments. Yet those objects give rise to shadowing, blocking, and diffraction, all of which are important in the design of wireless communication systems, especially at high frequencies, where channels are more directional and thus easily blocked [8]. The impact of blockage has been investigated extensively in the mmWave band (e.g., [9]-[12]); however, far fewer results are known in the THz regime. In [13], human body blockage and its mitigation are studied in an indoor scenario through numerical simulations. Ref. [14] investigates the attenuation provided by humans placed randomly in a simulated scenario where the blockage is modeled as a 4state Markov model. In [15], the blockage and diffraction produced by the human body are analyzed and modeled using a simple double-knife edge diffraction model at 73 GHz. Nonetheless, from a system point of view, blockage needs to be considered in the context of multipath propagation; depending on alternative propagation paths (beam directions), the effect of blockage can be mitigated significantly. Furthermore, apart from multipath propagation, the angular distribution with respect to the strongest path plays a significant role. Thus, such investigations must be considered in the context of the environment of interest and combine propagation and communication theory. To the best of our knowledge, this aspect of blockage at THz in a microcellular scenario has not yet been investigated.

Keeping all the discussion above in mind, in this paper, we aim to study the effects of blockers in microcellular scenarios based on our extensive double-directional microcellular channel measurements [6]. We study the mean and distribution of the attenuation faced by the line of sight (LOS) and non-LOS (NLOS) links as a result of blocking, relate it to the angular diversity, and draw conclusions toward eventual system design.

The rest of this paper is organized as follows: In Section II, we describe the measurement setup and sites. In Section III, we discuss the scenario under investigation and then present our key results in Section IV. Finally, we conclude the manuscript in Section V.

II. MEASUREMENT EQUIPMENT AND SITE

For the reader's convenience, we summarize the critical channel sounder settings and environment descriptions of our measurements; for details, please see [6].

A. Sounder and key settings

The microcellular measurement campaign was conducted using a frequency-domain channel sounder [4]–[6], [16]. The main component of the measurement system is a vector network analyzer (VNA) that scans the environment in the selected frequency range (145-146 GHz; 1001 points) by using frequency extenders and mechanically rotating horn antennas. Before processing and analysis, it is necessary to eliminate the frequency response of the 'system and antennas' from the measurement. For this purpose, we performed time-gated overthe-air (OTA) calibration every measurement day.

Since we are interested in *Microcells*, following the 3GPP recommendation [17] we placed the Tx at 11.5 m from the ground and the Rx at 1.7 m. The initial alignment for the antenna is set such that the azimuth angle $\phi = 0^{\circ}$ and the elevation angle $\tilde{\theta} = 0^{\circ}$ will correspond to the LOS for all points in the campaign (this holds even if the physical LOS or blocked). Both Tx and Rx scans are performed over three elevations separated 13° ($\tilde{\theta}_{Tx}$, $\tilde{\theta}_{Rx} \in \{-13^{\circ}, 0^{\circ}, 13^{\circ}\}$). The azimuthal scan of the Tx is taken over the range $[-60^{\circ}, 60^{\circ}]$ in 10° steps, corresponding to a typical base station (BS) microcell sector antenna. A complete scan from 0° to 360° in azimuth, with the same granularity as the Tx side, is performed at the Rx, where three elevations are also scanned.

B. Urban microcellar scenario

The measurements for the current campaign were performed at the University of Southern California (USC) University Park Campus in Los Angeles, California, USA. Fig. 1 shows a map of the measurement locations. The positioner was placed in 6 locations for Tx and 26 for Rx (13 LOS and 13 NLOS). In Tx's case, all sites are on the third level of the Downey Way Parking Structure (PSA) to have the height corresponding to a microcell as is needed in the scenario. On the other hand, the receiver locations are dispersed in multiple areas nearby the PSA building.

 Tx_1 was measured against 6 LOS points and 3 NLOS points; the LOS points are located on the Andrus Gerontology Building (GER) sidewalk. On the other side of the street, we have the Electrical Engineering Building (EEB), Ronald Tutor Hall (RTH), and Olin Hall of Engineering, creating a



Fig. 1: Microcellular campaign measurement scenario.

wide street canyon scenario. The NLOS points were under the entrance of the GER building. Tx_2 has 4 LOS points in the parking area surrounded by Ray Irani (RRI) and Michelson Hall (MCB). Tx_3 points were located on a sidewalk behind the USC Michelson Hall MCB. Tx_4 and Tx_5 points have 3 and 4 points, respectively. They are located in an alley between Technical Theatre Laboratory (TTL) and the Scene Dock Theatre (SCD) buildings emulating a street canyon. Route five is blocked by the roof and edge of the TTL building. Finally, Tx_6 has 3 NLOS points located on the sidewalk next to PSA. More details of the measurements are included in [6].

III. MODEL DESCRIPTION

A. Scenario of interest

As explained in the previous section, the measurements performed for this analysis were done in a microcellular scenario. These measurements were performed under "quasistatic" conditions (i.e., no moving objects in the environment) to capture the propagation characteristics of the environment. However, in actual microcellular environments, moving objects or blockers (e.g., pedestrians, buses, cars) interact dynamically with the user equipment (UE) and BS by obstructing partially or entirely the directions where paths are reaching the UE. Fig. 2 shows a sample scenario where the UE held by a pedestrian has a link to a BS blocked by a bus (red line); nevertheless, reflected paths from other objects (blue lines) provide additional paths reaching the BS. One of the most critical cases is when a blocker shadows the strongest path to the UE. An outage can be avoided if directional (beam) diversity is available from alternative propagation paths. Of course, this possibility must be exploited through a proper system design that adapts the beams, specifically by switching to one of the remaining paths in the scenario.

The current analysis will only focus on the UE (Rx) azimuth domain (i.e., blockers affect all elevations and all Tx directions at the same time) because it is less likely that an object can obstruct the BS (Tx) due to its height. Fig. 3 shows a sample blockage analysis where the blocker blocks the main beam and contiguous beams within an angular range of width γ . The blockers are assumed to be perfect absorbers ($A_{abs} = +\infty$ dB), i.e., they do not reflect nor allow transmission through them to any path hitting them. Finally, the impact of blockage

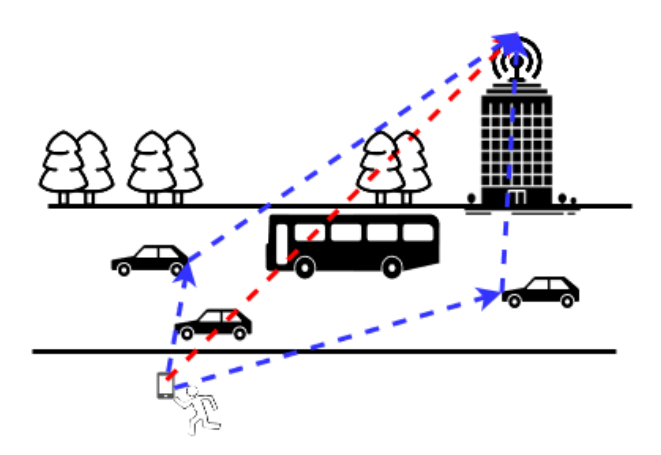


Fig. 2: Sample microcellular scenario.

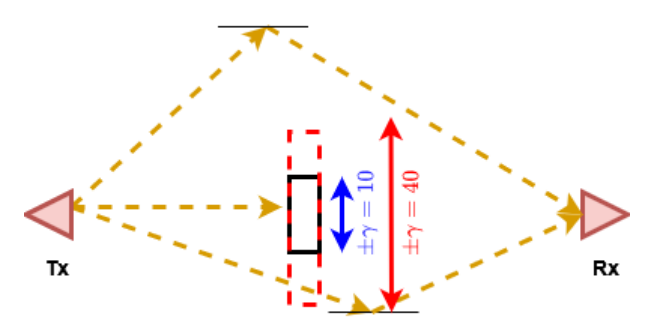


Fig. 3: Blocker analysis.

of multiple contiguous beams centered in the strongest one is analyzed.

B. Processing of channel data

For each Tx-Rx geographical location, the sounder produces a five-dimensional tensor $H_{meas}(f,\phi_{Tx},\tilde{\theta}_{Tx},\phi_{Rx},\tilde{\theta}_{Rx};d)$ where f denotes the frequency points over the 1 GHz bandwidth (145-146 GHz), ϕ_{Tx} and ϕ_{Rx} denote the azimuth orientation of the Tx and Rx antennas, respectively, $\tilde{\theta}_{Tx}$ and $\tilde{\theta}_{Rx}$ denote elevation orientation of the Tx and Rx antennas, respectively, and d is the Tx-Rx distance. The dimensions of the tensor, H_{meas} , are $N\times N_{Tx}^{\tilde{\theta}}\times N_{Tx}^{\phi}\times N_{Rx}^{\tilde{\theta}}\times N_{Rx}^{\phi}$ where N is the number of frequency points per sweep (1001), N_{Tx}^{ϕ} and N_{Rx}^{ϕ} are the number of azimuth directions at the Tx (13) and Rx (36), and $N_{Tx}^{\tilde{\theta}}$ and $N_{Rx}^{\tilde{\theta}}$ are the number of elevation directions at the Tx (3) and Rx (3), respectively.

As previously explained, we calibrate the measurements using an over-the-air (OTA) calibration to eliminate the effects of the system and antennas from the measurement captures [16]. This calibrated channel transfer function $(H(f,\phi_{Tx},\tilde{\theta}_{Tx},\phi_{Rx},\tilde{\theta}_{Rx};d))$ is the input for the processing analysis ¹. Using this channel frequency response (CFR), we compute the double-directional power delay profile (PDP) by:

$$P_{calc}(\tau, \phi_{Tx}, \tilde{\theta}_{Tx}, \phi_{Rx}, \tilde{\theta}_{Rx}; d) = |\mathcal{F}_f^{-1}\{H(f, \phi_{Tx}, \tilde{\theta}_{Tx}, \phi_{Rx}, \tilde{\theta}_{Rx}; d)\}|^2$$
(1)

where \mathcal{F}_f^{-1} is the inverse fast Fourier transform (IFFT) with respect to f. An essential issue to reduce is the impact of noise in delay bins; techniques, such as noise threshold and delay gating, are applied to $P_{calc}(\tau)$ [16].

C. Angular analysis

Our analysis is mainly focused on the angular domain; therefore, we take advantage of the *double-directional* response obtained per Tx-Rx pair to analyze the power distribution over the angles. The starting point for this analysis is the double-directional angular power spectrum, a function of the power concentration over different directions (particular azimuth, elevation directions) at Tx and Rx. The DDAPS is computed as the integration over τ of the *double-directional* response. Given the small number of elevation captures in both Tx and Rx (which was imposed by limits on the measurement duration) and also the fact they were captured with an angular spacing of one HPBW, we add the different contributions to get an *azimuthal* double directional APS (*DDAPS*) like [5], [6]. 2

Due to the typical geometry, i.e., BS (Tx in our case) is located higher up, with no blocking objects in the vicinity, while cars and other blockers can be close to the UE (Rx in our case). We focus on analyzing blockers on the Rx side. For this reason, we combine the azimuthal captures on the Tx side to have the Rx angular power spectrum (Rx APS). To measure the impact of the blocker in Rx APS, we assume the worst-case scenario when an object blocks the main beam in the Rx APS. A working system should choose the next strongest available beam if that occurs. Such an approach is performed, e.g., in mmWave systems in 5G NR, where the system retains a list of *fallback* beams it can transmit on if the strongest beam gets blocked [18], [19]. We define the variable Δ as the beam power difference before and after the blocker obstructs the main beam:

$$\Delta = \max(APS_{pre}(\phi_{Rx})) - \max(APS_{post}(\phi_{Rx}))$$
 (2)

where APS_{pre} is the Rx APS before the blockage and APS_{post} is the Rx APS after it. Note that this is *not* the attenuation experienced by the LOS beam, but rather the *effective* power reduction experienced by the system when considering ideal switching to the instantaneously best beam. To observe the total impact of the blocker, we obtain the power of the strongest beam after the blockage:

$$P_{MD}^{post} = \max\left(APS_{post}(\phi_{Rx})\right) \tag{3}$$

Finally, Δ, P_{MD}^{post} are modeled using a Gaussian CDF to study their behavior $\mathcal{N}(\mu, \sigma)$.

IV. RESULTS

In this section, we present the results of our analysis. Fig. 4 shows the DDAPS of a LOS point $(Tx_2 - Rx_{10})$, observing the LOS (strongest) direction is at $\phi_{Tx} = \phi_{Rx} = 0$. The

²Note that the use of this DDAPS in the blockage calculations implicitly assumes that the blockage affects all elevation angles uniformly. While this is fulfilled for most blockage scenarios, it might not be universally valid.

¹It will be called channel frequency response (CFR) from now on.

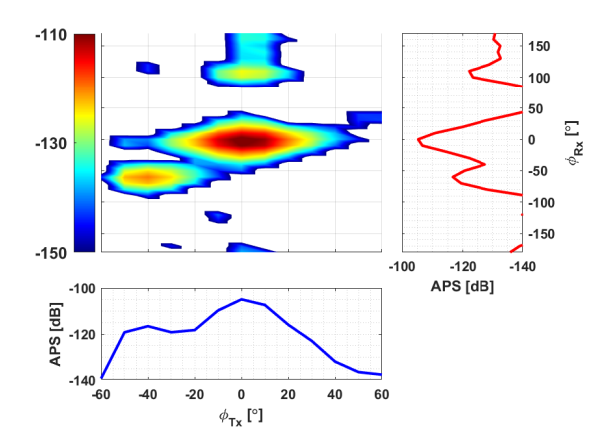


Fig. 4: $Tx_2 - Rx_{10}$ DDAPS, $d_{Tx-Rx} = 54.3$ m.

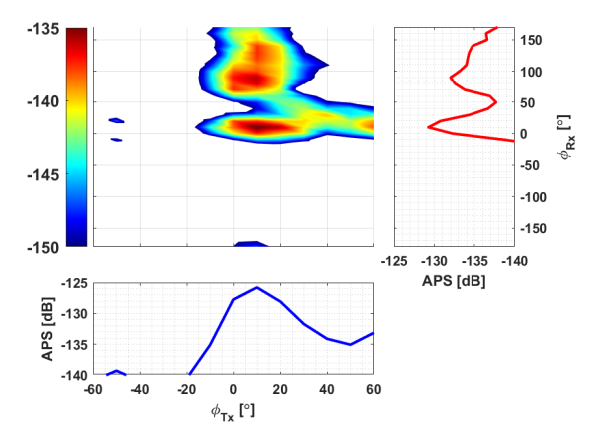


Fig. 5: $Tx_3 - Rx_{14}$ DDAPS, $d_{Tx-Rx} = 62.6$ m.

DDAPS shows a main beam wider than the beamwidth of the antennas we used in the measurements; thus, significant power is available in beam directions other than the LOS beam. Yet the power in these beams is of limited value for angular diversity since a blocking object might easily obstruct an angular range larger than the antenna beamwidth and thus suppress the power in those nearby beams. More useful is the fact that there are additional widely separated directions with considerable power. For instance, $\phi_{Tx} = -40, \phi_{Rx} = -60$ shows power only 10 dB lower than the LOS; another direction $\phi_{Tx} = 0, \phi_{Rx} = 110$ with 17dB less power than the LOS. From the Rx point of view, we have diversity (at least three different paths) within a 20dB dynamic range and four paths if the range is increased to 25 dB. Another sample DDAPS is shown in Fig. 5. In this NLOS scenario the strongest beam is pointing at $\phi_{Tx} = \phi_{Rx} = 10$, we have additional beams with considerable power such as $\phi_{Tx} = 10, \phi_{Rx} = 90,$ $\phi_{Tx} = 60, \phi_{Rx} = 20, \text{ and } \phi_{Tx} = 10, \phi_{Rx} = 150.$ Looking at the Rx APS, we observe multiple beams with strong power (within a 10dB dynamic range), indicating a large angular diversity for this scenario.

The following parameter to be analyzed is Δ , where Fig. 6 shows the CDF for this parameter in all the measurement points. For the LOS points, we conjecture that given the concentration of power in the LOS, if we block the strongest

TABLE I: $\bar{\Delta}$ value per route, LOS case.

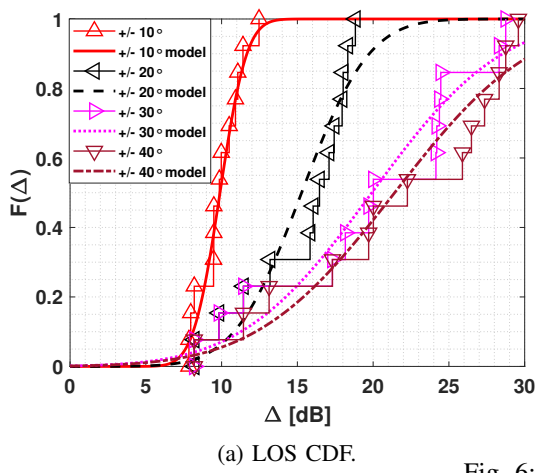
	$\pm \gamma = 10^{\circ}$	$\pm \gamma = 20^{\circ}$	$\pm \gamma = 30^{\circ}$	$\pm \gamma = 40^{\circ}$
Tx ₁	9.98	14.07	16.53	17.99
Tx ₂	9.96	15.97	23.18	23.75
Tx4	9.63	16.77	22.33	25.17

component, the relative attenuation will increase when the blockage covers more of the adjacent beams. As indicated above, due to the relatively broad beam of the antennas in our measurements ($HPBW=13^{\circ}$), only synthetically blocking the strongest beam would not obstruct the LOS direction³. On the contrary, an actual (physical) object blocking the LOS would not just block the LOS but instead its contribution to multiple beams; if we only considered the LOS direction blocked, the adjacent beams, with power levels close to the strongest beam, will make Δ small. For this reason, the analysis will start with a blockage that covers the strongest beam and $\pm \gamma = 10^{\circ}$.

We then analyze the CDF of Δ , where the CDF is taken over the ensemble of the different Tx/Rx pairs, which are placed in scenarios covering two street canyons and an open area in the selected environments. Fig. 6a shows the CDF for different values of angular blockage, where we note that such values are impacted by both the size of the blocking objects and their proximity to the UE. As the angular range increases, Δ starts with a mean value of 9.89 dB, reaching approximately 21 dB when an angular range ($\pm \gamma = 40^{\circ}$) around the LOS is blocked, similar to what we described earlier. The standard deviation increases from 1.39 dB for the single beam blockage to the most extensive case ($\pm \gamma = 40^{\circ}$) to 7.16 dB. In the street canyon scenario, we expect large concentrations of power along the LOS directions. Tx_1 has the Rx locations placed on one side of the street, buildings on the right side and the back (Parkside International Residential College (IRC) building, see Fig 1) of the Rx are primary reflectors in this scenario. For Tx_4 , the alley is narrower, so significant power contributions only come from the LOS; thus, a blocker in the LOS will have a considerable impact. Finally, in Tx_2 , the MCB and RRI buildings offer close reflectors observable in directions other than the LOS, like Fig. 4. This effect can be observed in Table I, where the mean values per route for the LOS case are shown.

In the NLOS case, one can anticipate that the blockage will have a less significant impact on the relative performance with and without a blocker than the LOS because of higher angular dispersion, i.e., multiple directions with comparable powers. The mean Δ value increases to approximately 10 dB for the case $\pm \gamma = 40^{\circ}$. In Tx_1 (NLOS), the Rx locations are inside the portico area; the observable path comes from the reflections of the RTH and EEB and the pillars of the GER building, indicating a significant number of directions with considerable energy. Tx_3 also shows several paths with significant power due to reflections from signs in the parking area, Kaprielian Hall (KAP), and the RRI buildings; for

³unless Tx-Rx distances are tiny, a case that does not occur in the analyzed measurements.



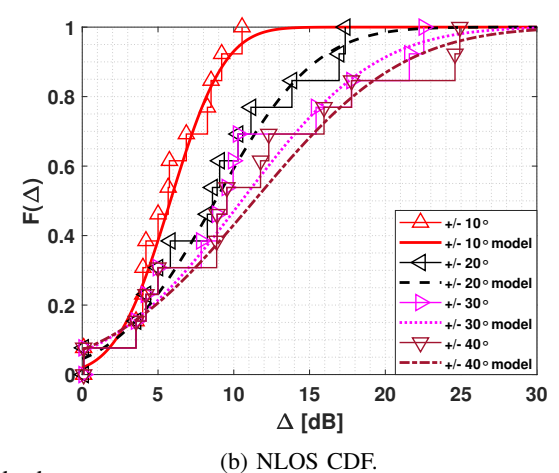


Fig. 6: Δ for both cases.

TABLE II: $\bar{\Delta}$ value per route, NLOS case

	$\pm \gamma = 10^{\circ}$	$\pm \gamma = 20^{\circ}$	$\pm \gamma = 30^{\circ}$	$\pm \gamma = 40^{\circ}$
Tx_1	5.14	8.11	8.27	8.94
Tx_3	2.62	2.62	2.62	2.62
Tx_5	8.06	11.94	15.66	16.88
Tx_6	6.71	11.4	13.8	15.09

instance, Fig. 5. Therefore, Δ for this route case should be the lowest of all NLOS routes, which is confirmed by the data in Table II. The opposite effect is observed in Tx_5 , a narrower street canyon, where the paths are highly concentrated in a segment of angles, similar to the LOS case. Thus, the blocker will produce a larger Δ . Finally, in the case of Tx_6 we have reflections from the nearby buildings and ground reflections offering additional paths to the receiver, lower than Tx_1 because of the distance between Tx and Rx (see Table III for estimated parameters).

It is essential to highlight that to assess the impact of a blocker thoroughly; it is necessary not only to analyze Δ , which can give the "impression" that NLOS points outperform LOS ones when a blocker obstructs the main beam, but rather the absolute received power as well. Therefore, we analyze the power of the strongest beam after the blockage to completely discern the blocker's impact. Observing Fig. 7, we see the CDF for both the LOS and NLOS cases where LOS points have, on average, a more considerable gain than the NLOS points, even though Δ values exhibit the opposite behavior. In Table IV, we observe the values of P_{MD}^{post} , where the difference between LOS and NLOS starts from approximately 12 dB when the blockage only obstructs $\pm \gamma = 10^\circ$ the main beam to 6dB for the $\pm \gamma = 40^\circ$ case.

V. CONCLUSIONS

In this paper, we presented the results of an angular analysis of the impact of blockers on THz systems in urban microcellular scenarios at 145 GHz. The campaign used for the study includes LOS and NLOS measurements with distances between 18 and 83 m. Some of the key takeaways of this analysis are that the mean attenuation provided by a blocker

(i.e., Δ) is more prominent in LOS than NLOS points because of the higher concentration power in the LOS components. The attenuation increases when a blocker obstructs multiple beams, where the difference is reduced because the power received from different directions has an impact when the main beam is attenuated. Finally, even though the effects of the blocker are more pronounced in LOS cases, the power of the strongest beam after the blockage is still larger in LOS than in NLOS cases. These results help design algorithms or systems, such as beamforming or intelligent reflective surfaces, that can overcome communications in the THz band when a blocker (e.g., pedestrians, cars, buses) obstructs the strongest path at the receiver.

ACKNOWLEDGMENT

This work was partly supported by the Semiconductor Research Corporation (SRC) under the ComSenTer program, NSF, NIST, Samsung Research America, and the Foreign Fulbright Ecuador SENESCYT Program.

REFERENCES

- [1] H. Tataria, M. Shafi, A. F. Molisch, M. Dohler, H. Sjöland, and F. Tufvesson, "6g wireless systems: Vision, requirements, challenges, insights, and opportunities," *Proceedings of the IEEE*, vol. 109, no. 7, pp. 1166–1199, 2021.
- [2] Z. Chen, X. Ma, B. Zhang, Y. Zhang, Z. Niu, N. Kuang, W. Chen, L. Li, and S. Li, "A survey on terahertz communications," *China Communications*, vol. 16, no. 2, pp. 1–35, 2019.
- [3] C. Han, Y. Wang, Y. Li, Y. Chen, N. A. Abbasi, T. Kürner, and A. F. Molisch, "Terahertz wireless channels: A holistic survey on measurement, modeling, and analysis," arXiv preprint arXiv:2111.04522, 2021.
- [4] N. A. Abbasi, A. Hariharan, A. M. Nair, A. S. Almaiman, F. B. Rottenberg, A. E. Willner, and A. F. Molisch, "Double directional channel measurements for thz communications in an urban environment," *ICC* 2020-2020 IEEE International Conference on Communications (ICC), pp. 1–6, 2020.
- [5] N. A. Abbasi, J. Gomez-Ponce, R. Kondaveti, S. M. Shaikbepari, S. Rao, S. Abu-Surra, G. Xu, C. Zhang, and A. F. Molisch, "Thz band channel measurements and statistical modeling for urban d2d environments," *IEEE Transactions on Wireless Communications*, pp. 1–1, 2022.
- [6] N. A. Abbasi, J. Gomez-Ponce, R. Kondaveti, A. Kumar, E. Bhagat, R. N. Rao, S. Abu-Surra, G. Xu, C. Zhang, and A. F. Molisch, "Thz band channel measurements and statistical modeling for urban microcellular environments," arXiv preprint arXiv:2112.01770, submitted to IEEE Transactions, Jan 2022.

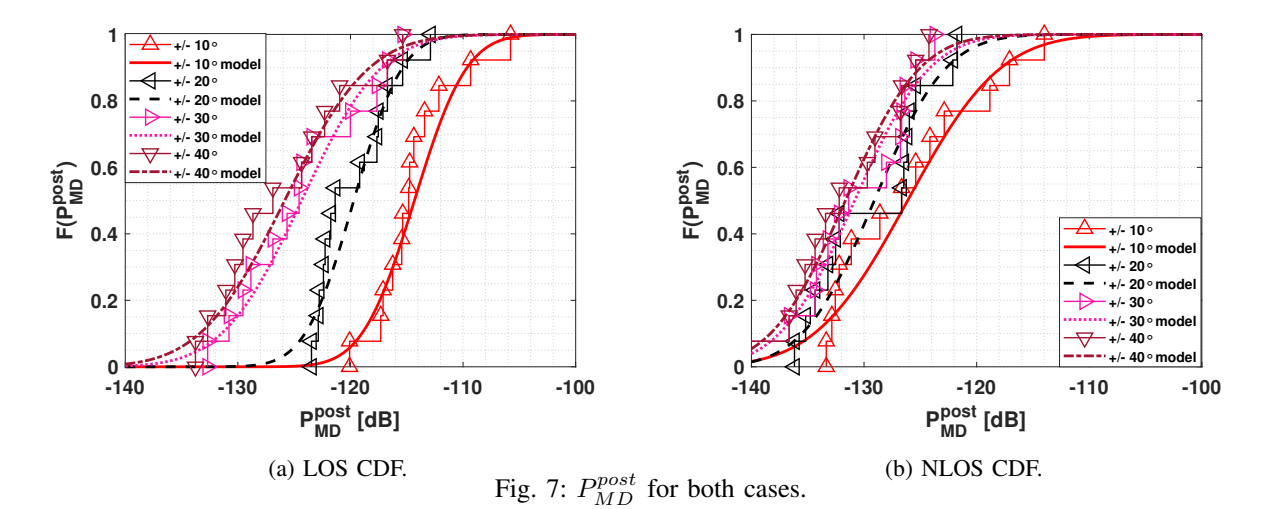


TABLE III: Δ parameters with 95% confidence interval for all points.

γ	$\bar{\Delta}^{LOS}$	$ar{\Delta}_{CI}^{LOS}$	$\bar{\Delta}^{NLOS}$	$ar{\Delta}_{CI}^{NLOS}$	$S\{\Delta^{LOS}\}$	$S\{\Delta_{CI}^{LOS}\}$	$S\{\Delta^{NLOS}\}$	$S\{\Delta_{CI}^{NLOS}\}$
±10°	9.89	{9.06, 10.73}	1.39	{1, 2.29}	5.82	{4.11, 7.53}	2.82	{2.03, 4.67}
±20°	15.28	{13.17, 17.38}	3.49	{2.5, 5.75}	8.78	{5.65, 11.9}	5.17	{3.71, 8.47}
±30°	19.92	{15.84, 23.99}	6.74	{4.84, 11.14}	10.51	{6.31, 14.72}	6.97	{5, 11.5}
±40°	21.42	{17.1, 25.74}	7.16	{5.13, 11.81}	11.34	{6.67, 16.02}	7.73	{5.54, 12.76}

TABLE IV: P_{MD}^{post} parameters with 95% confidence interval for all points.

γ	\bar{P}^{LOS}	$ar{P}_{CI}^{LOS}$	\bar{P}^{NLOS}	\bar{P}_{CI}^{NLOS}	$S\{P^{LOS}\}$	$S\{P_{CI}^{LOS}\}$	$S\{P^{NLOS}\}$	$S\{P_{CI}^{NLOS}\}$
±10°	-114.32	{-116.53, -112.12}	3.65	{2.62, 6.02}	-126.13	{-130, -122.21}	6.49	{4.65, 10.71}
±20°	-119.71	{-121.45, -117.66}	3.38	{2.43, 5.59}	-129.09	{-132.12, -126.07}	5	{3.59, 8.26}
±30°	-124.34	{-127.7, -120.99}	5.55	{3.99, 9.16}	-130.83	{-133.99, -127.67}	5.23	{3.75, 8.63}
±40°	-125.85	{-129.41, -122.29}	5.89	{4.23, 9.73}	-131.66	{-134.8, -128.51}	5.2	{3.73, 8.58}

- [7] Y. Xing and T. S. Rappaport, "Propagation measurements and path loss models for sub-thz in urban microcells," in ICC 2021 - IEEE International Conference on Communications, 2021, pp. 1–6.
- [8] L. You, X. Chen, X. Song, F. Jiang, W. Wang, X. Gao, and G. Fettweis, "Network massive mimo transmission over millimeter-wave and terahertz bands: Mobility enhancement and blockage mitigation," *IEEE Journal on Selected Areas in Communications*, vol. 38, no. 12, pp. 2946–2960, 2020.
- [9] J.-J. Park, J. Lee, J. Liang, K.-W. Kim, K.-C. Lee, and M.-D. Kim, "Millimeter wave vehicular blockage characteristics based on 28 ghz measurements," in 2017 IEEE 86th Vehicular Technology Conference (VTC-Fall), 2017, pp. 1–5.
- [10] T. Choi, C. U. Bas, R. Wang, S. Hur, J. Park, J. Zhang, and A. F. Molisch, "Measurement based directional modeling of dynamic human body shadowing at 28 ghz," in 2018 IEEE Global Communications Conference (GLOBECOM), 2018, pp. 1–6.
- [11] C. Slezak and S. Rangan, "Measurement-based indoor millimeter wave blockage models," *IEEE Transactions on Wireless Communications*, pp. 1–1, 2022.
- [12] U. T. Virk and K. Haneda, "Modeling human blockage at 5g millimeterwave frequencies," *IEEE Transactions on Antennas and Propagation*, vol. 68, no. 3, pp. 2256–2266, 2020.
- [13] B. A. Bilgin, H. Ramezani, and O. B. Akan, "Human blockage model for indoor terahertz band communication," in 2019 IEEE International Conference on Communications Workshops (ICC Workshops). IEEE, 2019, pp. 1–6.
- [14] S. Ju, O. Kanhere, Y. Xing, and T. S. Rappaport, "A millimeter-wave channel simulator nyusim with spatial consistency and human blockage," in 2019 IEEE Global Communications Conference (GLOBECOM), 2019, pp. 1–6.
- [15] G. R. MacCartney, S. Deng, S. Sun, and T. S. Rappaport, "Millimeterwave human blockage at 73 ghz with a simple double knife-edge

- diffraction model and extension for directional antennas," in 2016 IEEE 84th Vehicular Technology Conference (VTC-Fall), 2016, pp. 1–6.
- [16] J. Gomez-Ponce, N. A. Abbasi, A. E. Willner, C. J. Zhang, and A. F. Molisch, "Directionally resolved measurement and modeling of thz band propagation channels," *IEEE Open Journal of Antennas and Propagation*, vol. 3, pp. 663–686, 2022.
- [17] 3GPP, "5G; Study on channel model for frequencies from 0.5 to 100 GHz," 3rd Generation Partnership Project (3GPP), Technical Specification (TS) 38.901, 05 2017, version 14.0.0. [Online]. Available: https://www.etsi.org/deliver/etsi_tr/138900_138999/138901/ 14.00.00_60/tr_138901v140000p.pdf
- [18] E. Dahlman, S. Parkvall, and J. Skold, 5G NR: The next generation wireless access technology. Academic Press, 2020.
- [19] S. Hur, H. Yu, J. Park, W. Roh, C. U. Bas, R. Wang, and A. F. Molisch, "Feasibility of mobility for millimeter-wave systems based on channel measurements," *IEEE Communications Magazine*, vol. 56, no. 7, pp. 56–63, 2018.